Variability of morphology in photoplethysmographic waveform quantified with unsupervised wave-shape manifold learning for clinical assessment

Yu-Chieh Ho[1,2], Te-Sheng Lin[1,2], Shen-Chih Wang[3,4], Chen-Shi Chang[5], Yu-Ting Lin[3,4,*]

Abstract

Objective: We investigated fluctuations of the photoplethysmography (PPG) waveform in patients undergoing surgery. There is an association between the morphologic variation extracted from arterial blood pressure (ABP) signals and short-term surgical outcomes. The underlying physiology could be the numerous regulatory mechanisms on the cardiovascular system. We hypothesized that similar information might exist in PPG waveform. However, due to the principles of light absorption, the noninvasive PPG signals are more susceptible to artifacts and necessitate meticulous signal processing. *Approach:* Employing the unsupervised manifold learning algorithm, Dynamic Diffusion Map, we quantified multivariate waveform morphological variations from the PPG continuous waveform signal. Additionally, we developed several data analysis techniques to mitigate PPG signal artifacts to enhance performance and subsequently validated them using real-life clinical database. *Main results:* Our findings show similar associations between PPG waveform during surgery and short-term surgical outcomes, consistent with the observations from ABP waveform analysis. *Significance:* The variation of morphology information in the PPG waveform signal in major surgery provides clinical meanings, which may offer new opportunity of PPG waveform in a wider range of biomedical applications, due to its non-invasive nature.

Keywords: photoplethysmography waveform, liver transplant, manifold learning, dimension reduction, signal processing

1. Introduction

The human cardiovascular system fluctuates over time, hence the variation of its signal waveform. Focusing on the arterial blood pressure (ABP) waveform, studies have reported that within the tens of thousands of ABP pulses from a patient undergoing

*Corresponding author
Email address: linyuting@hotmail.com.tw (Yu-Ting Lin)
[1]National Center for Theoretical Sciences, National Taiwan University, Taipei 106, Taiwan
[2]Department of Applied Mathematics, National Yang Ming Chiao Tung University, Hsinchu 300, Taiwan
[3]Department of Anesthesiology, Taipei Veterans General Hospital, Taipei 112, Taiwan
[4]School of Medicine, National Yang Ming Chiao Tung University, Taipei 112, Taiwan
[5]Department of Anesthesiology, Shin Kong Wu Ho Su Memorial Hospital, Taipei 111, Taiwan

prolonged surgery, no two pulses are identical in terms of waveform morphology [1, 2, 3]. Information extracted from its dynamic and complex morphology has also proven valuable for various applications in clinical medicine [4, 5, 6, 7, 8]. While the morphology of an ABP waveform cycle is influenced by wave reflections of the blood flow from the heart to the whole vascular tree in the human body [9], the *variation of morphology* (*varM*) could reflect numerous interactions between various physiological mechanisms constantly regulating the cardiovascular system [10]. We have recently reported its relationships with the patient's clinical condition.

The calculation of ABP varM leverages the Dynamic Diffusion Map (DDMap) algorithm, an unsupervised manifold learning technique developed to tackle the multivariate nature of cardiovascular waveform morphology [2, 11, 3]. This method reveals the relationship between high-dimensional data points in a low-dimensional Euclidean space by constructing a weighted graph between data points and leveraging the eigensystem of a random walk on the graph. By treating each segment of the waveform within a heart-beat cycle as a data point in high-dimensional space, DDMap unveils the hidden structure of the data, facilitating the observation and quantification of varM information. Notably, the DDMap algorithm possesses the ability to reveal non-linear internal structures and demonstrate robustness in statistical analysis [3, 12].

The use of the DDMap to analyze ABP waveform data during liver transplant surgery revealed an association between varM and the condition of patients undergoing liver transplant surgery, as well as their short-term surgical outcomes [10]. Building upon this finding and the existing literature on ABP waveform analysis [10, 3, 11], we hypothesized that a similar quantitative assessment of varM could be derived from the photoplethysmographic (PPG) pulse wave [13].

PPG is different to ABP in the physical principal, while sharing similar pulsatile waveform pattern [14, 15, 16, 17]. The invasive intra-arterial blood pressure measurement allows for direct pressure measurement as well as waveform information in absolute unit via the connecting pipe principle. Hence, ABP waveform information has been used to assess various hidden conditions of the cardiovascular system [8, 2, 5]. On the other hand, non-invasive PPG relies on the relative differences in light absorption at different wavelengths, which requires frequent automatic adjustment in the signal processing stage to obtain the arterial oximeter and the pulsation waveform displayed on the monitor. Therefore, while the oximeter readings are indispensable in various situations of the clinical medicine, PPG waveform is more susceptible to interference from various external factors and generally considered to be less reliable [18].

The PPG signal is susceptible to various types of artifacts [16, 19, 20], this includes variations in baseline and intensity of pulse dynamics caused by motion artifact and probe-tissue interface disturbance [14], unavoidable noise and external interference during signal recording (Figure 1(a)), and pulse dispersion within a patient's signal after segmentation due to dynamic physiological conditions (Figure 1(b)). Technical factors such as the type of sensor used and the measurement site location can also affect the waveform [19, 21]. To elaborate on the pulse dispersion issue depicted in Figure 1(b), the ideal scenario involves pulses from a signal aligning neatly at the black dash line after signal segmentation to focus our analysis on waveform morphology, as shown in the left image of Figure 1(b). However, dispersion may occur in some instances, as illustrated in the right image of Figure 1(b).

Nonetheless, our shift in focus from ABP to PPG is driven by the recognition that

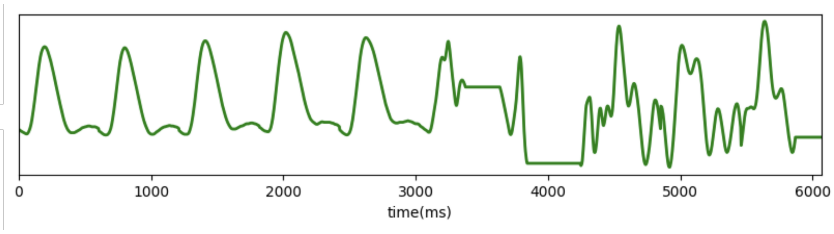

(a) Example of a PPG signal with interferes by external factors.

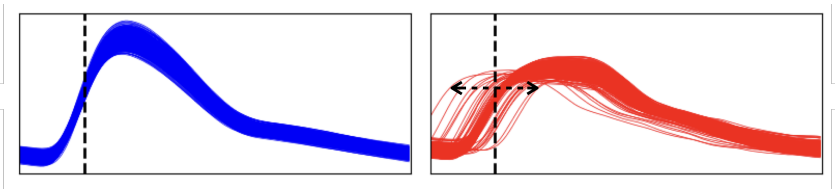

(b) Example of two PPG waveforms with diverse pulse dispersion after signal segmentation. In the left panel, pulses align well at the black dash line, whereas in the right panel, pulses are dispersed along the line.

Figure 1: Illustration of artifacts in PPG signals.

non-invasive and ubiquitous PPG, as opposed to the direct intra-arterial blood pressure waveform exclusively in the operating room or the critical care unit in the hospital, could grant applications to wider biomedical situations [14, 15, 22, 23]. However, extracting reliable information from the PPG remains critical to achieve comparable results to ABP monitoring, given the numerous challenges in signal analysis. Our study prioritizes the development of methodologies to address these influences, followed by an evaluation of the effectiveness of PPG varM in relation to clinical data.

The rest of the manuscript is organized as follows. Section 2 provides a detailed explanation of the procedure, starting from the acquisition of the original PPG signal to the quantification of signal morphology, along with the techniques employed to address the PPG signal artifact problems. In Section 3, we present the relationships observed between the quantified varM and the post-surgery clinical score system. Further discussion of the results is presented in Section 4, followed by the conclusion and acknowledgments in Sections 5 and 6, respectively.

2. Methodology

In this section, we elaborate the standard procedure for quantifying varM and the techniques employed to address PPG signal artifacts. In Section 2.1, the collected PPG waveform is preprocessed in order to facilitate the application of the DDMap algorithm, which is thoroughly elucidated in Section 2.2. Following this, Section 2.3 outlines our approach to quantifying waveform morphology, while Section 2.4 provides a summary of the standard procedure for obtaining quantitative varM. Additionally, techniques aimed at mitigating the influence of signal artifacts and enhancing performance are discussed in

Section 2.5. Lastly, statistical analysis and sensitivity analysis between the varM and the clinical scores systems is presented in Section 2.6 and Section 2.7, respectively.

2.1. Preprocessing of PPG waveform

The continuous physiological waveform dataset was collected from a single center prospective observational study between 2018 and 2021 in Taipei Veterans General Hospital, Taipei, Taiwan. 85 living donor liver recipients were recruited after Institutional Review Board approval (IRB No.: 2017-12-003CC and 2020-08-005A) and written informed consent obtained from each patient. The four signals of these 85 cases, including ABP, PPG, central venous pressure (CVP), and electrocardiogram (ECG), were collected from the patient monitor (GE CARESCAPE^{TM} B850, GE Healthcare, Chicago, IL) via the data collection software S5 Collect (GE Healthcare). This study places its focus on the PPG signal to assess its performance in comparison to the ABP signal.

To obtain the waveform morphology each pulse from a continuous PPG waveform at a 300 Hz sampling rate, each pulse is automatically identified with the fiducial point as the maximum of the first difference of the anacrotic phase, the ascending part of the pulse. To obtain a waveform segment of each pulse including the anacrotic phase and dicrotic phase (as shown in Fig 3), we designed 130 ms before the fiducial point as the beginning of the pulse until the beginning of the next incoming pulse. The whole pulse waveform could be isolated accordingly in most situations. To handle the inevitable noise on the signal data, legitimate pulse is determined automatically with a two-pass algorithm with the conditions including peak maximum (10), the trough minimum (-5), the pulse width measured at height of fiducial point (600 ms), the minimal pulse width at the height of fiducial point (70 ms), the minimal duration to the previouse pulse (300 ms). These thresholds (initial values in parentheses) would be adjusted automatically by a feedback mechanism. Note these values might not be applicable to PPG signal data from the equipment of different manufacturer as PPG signal data do not possess standard unit.

Subsequently, pulses whose maximum is more than twice or whose minimum is less than twice the average pulse range, or pulses that contain long straight lines (indicating that no signal is detected for a long time) are regarded to be of poor quality. These pulses are automatically identified, removed, and replaced using linear interpolation relative to their temporal position. To specify the replacement step more fully, we let Z be the removed pulse with time location t, Z_x be the nearest qualified pulse of Z with time location $t_x < t$, and Z_y be the nearest qualified pulse of Z with time location $t_y > t$. Then, Z is replaced by $\left(\frac{t_y - t}{t_y - t_x}\right) Z_x + \left(\frac{t - t_x}{t_y - t_x}\right) Z_y$. Furthermore, each pulse is subtracted by its median as the baseline, then divided by its ℓ^2-norm to increase its varM and decrease the difference between pulses made by artifacts when recording the waveform. Lastly, to adapt DDmap in the subsequent step, we need to calculate distances between pulses. We learned from previous studies [2, 10] that it is important to preserve the temporal structure within the pulse profile. Therefore rather than scaling or stretch it, we choose to truncate the tail so the pulses have equal length. The average PPG length was 207 ms while the truncating length was 467 ms. It deserves to be mentioned that from the perspective of cardiovascular physiology, each pulse is inevitably interrupted by the next incoming pulse driven from the next heart beat. This naturally occurred pulse waveform truncation is not uniform in length (time duration) since the heart beat intervals present variation. In this stage of affinity matrix construction, We made them truncated uniformly

Algorithm 1 The pseudo-code of the Dynamic Diffusion Map (DDMap).

Input: $X = \{x_i\}_{i=1}^n,\ q \in \mathbb{N}$.
Output: $\Psi = \{\Psi_i\}_{i=1}^n \subset \mathbb{R}^q$.

1: Construct an affinity matrix $W_{ij} = \exp(-\frac{\|x_i - x_j\|_{\ell^2}^2}{\varepsilon})$ $x_i \in X$, and ε is the 25-th percentile of all pairwise points in X.
2: Construct a diagonal matrix D where D_{ii} is the i-th row sum of W.
3: Compute the SVD of $D^{-1}W = U\Lambda V^T$. Preserve only the $(q+1)$-largest eigenpairs, then discard the largest one.
4: Construct the DDMap embedding $\Psi_i : x_i \to e_i^T U\Lambda$ for $i = 1, 2, ..., n$.

to offer a standard condition to preserve the subtle waveform morphologic information into the affinity matrix.

Following the pre-processing steps described above, we eliminated signal artifacts related to misaligned pulse baselines between cases, as well as shortages and divergences in pulse dynamics. However, challenges persist in mitigating the modulation of pulse waveform due to unavoidable transient noise in the signal (Fig 1(a)). Moreover, dynamic physiological conditions may frequently result in atypical shapes in the ascending part of the pulse (Fig 1(b)), a phenomenon encountered more often than in our previous ABP waveform analysis [10]. This complexity further complicates the identification of the systolic phase mentioned earlier. These technical issues will be will be discussed in more detail in the subsequent paragraphs.

2.2. Unsupervised manifold learning technique

The successive changes in pulse morphology within each heartbeat cycle are too subtle and sophisticated to be observed with the naked eye. Accordingly, we treat each pulse as a high-dimensional data point and utilize DDMap [11] to find a low-dimensional representation of the point cloud to visualize the relationships of all the pulses in high-dimensional space. Denoting the data set as $\{x_i\}_{i=1}^n$, the pseudo-code of the DDMap algorithm is presented in Algorithm 1. In the algorithm, only one parameter q needs to be selected, which determines the dimension of DDMap embedding. We empirically set $q = 15$. Note that our input dataset X is a pulse sequence, so the output embedding Ψ informs the time sequence of pulses, which allows us to analyze waveform dynamics using DDMap embedding trajectories evolving over time.

The DDMap algorithm works as follows. In step 1, we construct the affinity matrix based on a weighted graph formed on the high-dimensional dataset, where an edge is close to 1 if its endpoints are close to each other in the high-dimensional space, and is close to 0 otherwise. In step 2, we build a diagonal matrix whose diagonal elements are the row sums of the affinity matrix. In step 3, we perform a singular value decomposition on the matrix $D^{-1}W$ and use it to form the embedding of step 4.

The matrix $D^{-1}W$ in step 3 is a transition matrix (Markov chain), since all of its entries are nonnegative and all of its rows sum to 1. Note that the ij-th element of a transition matrix represents the probability of transition in one time step from x_i to x_j on the graph, $p(x_i, x_j)$. Now, we obtain the *diffusion distance (DDist)* pertaining to

DDMap, as

$$DDist(x_i, x_j) := \sqrt{\sum_{x_k \in X} \|p(x_i, x_k) - p(x_k, x_j)\|^2}. \tag{1}$$

$DDist(x_i, x_j)$ is small when there is a large number of short paths on the graph that connect x_i and x_j, and vice versa. The diffusion distance can be directly linked to the spectral properties as

$$DDist(x_i, x_j) = \|e_i^T U\Lambda - e_j^T U\Lambda\|. \tag{2}$$

Note that the eigenvalues of $D^{-1}W$ is $1 = \lambda_1 > \lambda_2 \geq \lambda_3 \cdots \geq \lambda_n \geq -1$, the eigenvector corresponding to eigenvalue 1 is a constant vector, and an eigenvalue reflects the importance of its corresponding eigenvector. Therefore, we may discard the first eigenvector and choose a proper q to embed the dataset into a much lower-dimensional euclidean space. Once we build the embedding as in step 4, we actually obtain an embedding such that the euclidean distance between pairwise points in the low-dimensional space is roughly equal to the $DDist$ between those points.

In the case when a dataset contains clusters with different densities, which most of the real-world dataset does, an affinity matrix using a global bandwidth in the DDMap algorithm may fail to present the real connectivity between points. To avoid this, local-scaling bandwidths [24] is used to construct a better affinity matrix instead. That is, we change ε in step 2 of Algorithm 1 to $\|x_i - x_s\|_{\ell^2}$, where $x_s \in X$ is the s-th nearest neighbor of x_i. Following the suggestion in [24] and taking into account the size of our dataset, we choose $s = 15$ when using Algorithm 1 with local-scaling. Figure 2 illustrates the difference between using a global bandwidth and local-scaling bandwidths in an affinity matrix. It is observed that the affinity between the blue points is stronger with local scaling compared to global scaling, and that the affinity between red points and blue points is relatively weaker. In this case, we can easily separate two groups of points using DDMap algorithm since both groups are strongly connected inside the groups and are poorly connected between two groups. From here on, when we mention the DDMap algorithm or the DDMap embedding, we means the algorithm 1 with local scaling and its' result.

2.3. Calculation of varM

The DDMap embedding and its trajectory provides a concise overview of the complex dynamical evolution. We further apply a moving median followed by a moving mean filter to obtain the trend of trajectory. Suppose a case has L pulses and its embedding points are $\{\Phi_i\}_{i=1}^L$, then the trend T of the embedding is

$$T_i = \frac{1}{k} \sum_{m=i-k+1}^{i} \text{median}(\Phi_{m-(k+1)/2}, ..., \Phi_{m+(k+1)/2}) \quad \text{for } i = 1, ..., L, \tag{3}$$

where k is chosen manually. Note that those Φ_i with $i < 1$ or $i > L$ were removed from the median pool, same as for m. The fraction in front of the summation depends on the number of m that are summing up.

Figure 3 demonstrates the process from continuous waveform to new representations (DDMap embedding) of consecutive pulses. The original continuous waveform is shown in panel (a), the preprocessed waveform is shown in (b), and the embedded waveform is

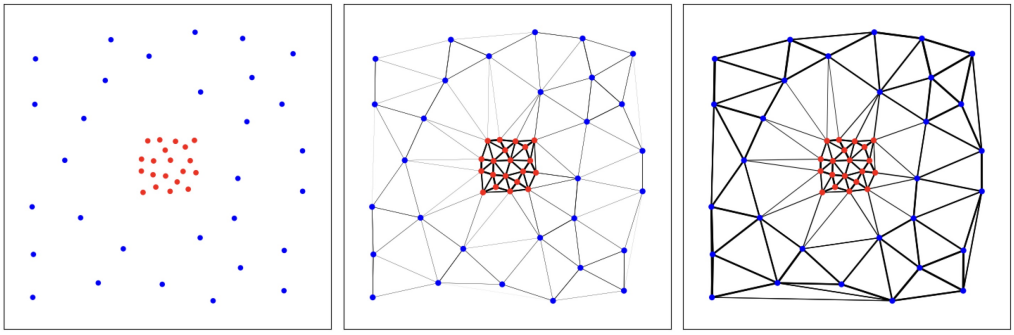

Figure 2: Illustration of the difference between using global scaling or local scaling in constructing an affinity matrix. Left: A dataset containing two groups of points (red and blue) with different densities. Middle: Affinities between data points using global scaling. The black line between pairwise points represent the affinity between them. The thicker it is, the stronger the affinity between those pairwise points are, vice versa. Right: Affinities between data points using local scaling.

shown in (c). Notably, the blue case has Meld_Na score of 56, while the red case has Meld_Na score of 5. In figure 3(c), it is observed that a case with a high Meld_Na score does not manifest intense dynamical evolution of pulses, resulting in a slow evolution of trend points. Conversely, a case with a low Meld_Na score displays a more complex dynamical change, leading to a rapid evolution of trend points. Quantifying the dynamical evolution of trend points may unveil its correlation with the post-surgery clinical score system.

By leveraging the DDMap embedding trajectory and its trend, we obtain the change of T for each case,

$$\mathrm{TS} := \frac{1}{L-1}\sum_{i=2}^{L}\|T_i - T_{i-1}\|, \tag{4}$$

which captured the slow-vary drift, is calculated as the mean of distances between each consecutive trend points, quantifying how fast the trend evolves. The trend speed (TS) measures are intuitively derived from the trajectory structure to assess the amount of waveform dynamics.

The trend preserved the relative slow movement component that is more relevant to the inner dynamics of the cardiovascular system according to our previous study [10]. As the fast movement part is often elicited by the variation of the venous blood returning to the heart due to respiratory cycle, arrhythmia such as premature contracture, atrial fibrillation, or even the transient motion artifact at the signal acquisition stage, the physiological regulation mechanisms exert controls on the cardiovascular system at the time scale longer than the breathing cycle [9].

2.4. Standard procedure of obtaining varM

First of all, we preprocess the PPG waveform into consecutive pulses as we described in Section 2.1. One case is removed due to the shortness of pulse length after trimming,

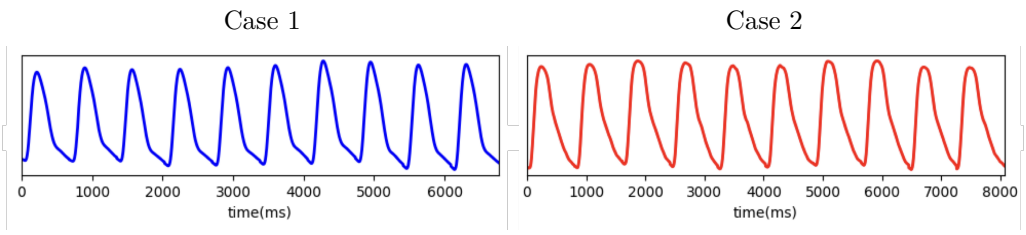

(a) Continuous waveform before preprocessing.

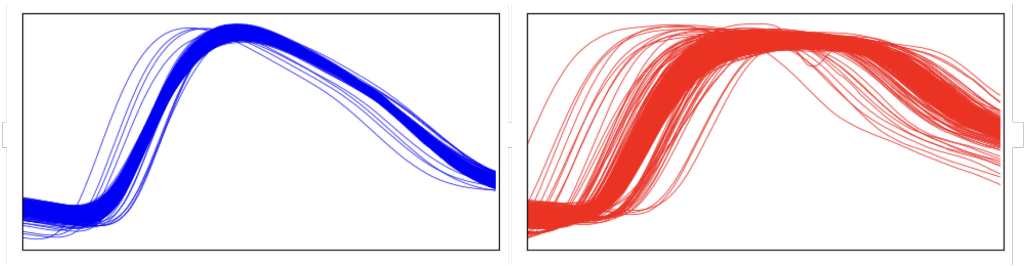

(b) Consecutive pulses after preprocessing.

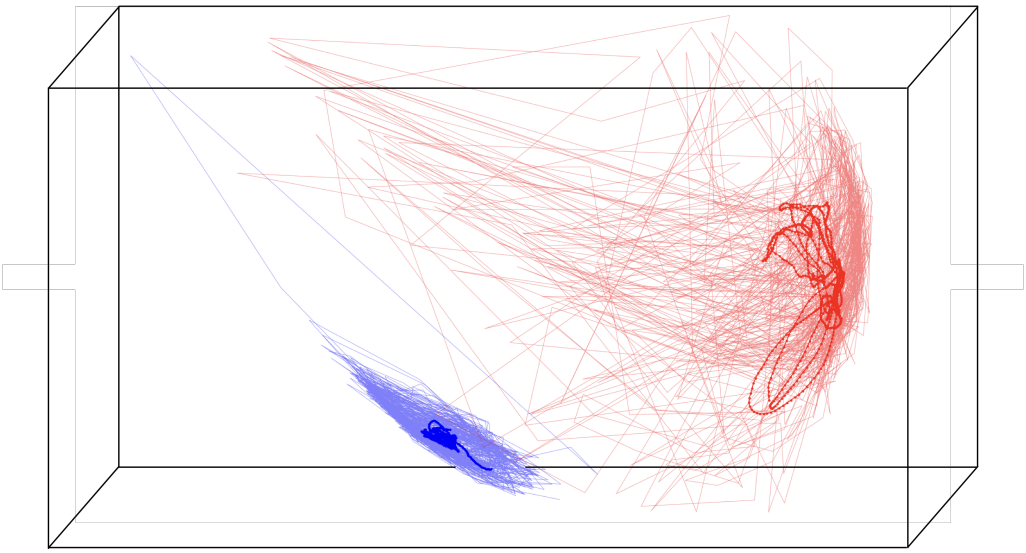

(c) DDMap embedding of two cases. The light color paths indicate the trajectories, and the dark color paths indicate the trends.

Figure 3: A visualization depicting the original signals of two cases without preprocessing, the beat-to-beat pulses after preprocessing, and their DDMap embedding alongside the trajectories and trends.

and two cases are removed since they do not have enough legitimate pulses. Accordingly, there are 82 cases of neohepatic phase.

To make the quantitative indices comparable and convenient in future applications, we use 85 cases of presurgical PPG data as reference baseline dataset as before [10].

For pulses of neohepatic phase of each case, we consider them as a non-baseline dataset and compute them individually. A dataset that combines the baseline dataset and a non-baseline dataset is formed, and a DDMap embedding that contains embedding of baseline dataset and non-baseline dataset is obtained by running the DDMap algorithm. Then, we compute the trends and varM of baseline dataset and non-baseline dataset. To rescale varM of the final non-baseline dataset, we consider the formula

$$\mathrm{varM}^* = \frac{\mathrm{varM} - \mathrm{median(pool\ of\ TS)}}{\mathrm{IQR(pool\ of\ TS)}} \times 25 + 60, \tag{5}$$

where pool of TS contains all varM of the baseline dataset, and IQR is the abbreviation for interquartile range.

2.5. Techniques and approaches for addressing PPG signal artifacts

Regarding noise effects and beat-to-beat pulses dispersion that cannot be eliminated by the standard procedure, we additionally consider two techniques to address them. The first approach is to replace the Euclidean distance $d(x_i, x_j) = \|x_i - x_j\|_{\ell^2}$ with the Wasserstein-1 distance $d_{w_1}(x_i, x_j)$ [25] in step 2 of Algorithm 1, which is out of consideration for removing the dispersion characteristic. The second technique is to employed the Hamming window [26] in the signal preprocessing step, which deal with both noise and dispersion artifacts.

The Hamming window is defined as

$$W_i := 0.54 - 0.46 \cos\left(2\pi\left(\frac{i}{w-1} + \frac{1}{2}\right)\right), \tag{6}$$

where $-\frac{w-1}{2} \leq i \leq \frac{w-1}{2}$, w is an odd number. Suppose the neohepatic phase of a case has pulses $\{x_i\}_{i=1}^{L}$, then applying the Hamming window to this case means to replace each pulse x_i by $\frac{1}{w}\sum_{j=-(w-1)/2}^{(w-1)/2} W_j x_{i+j}$. Note that those x_{i+j} with $i+j < 1$ or $i+j > L$ were removed from the summation. The fraction in front of the summation depends on the number of j that are summing up. Figure 4(a) shows the effect of the Hamming window on pulses. This technique reduces the signal noise and dispersion by considering not only the pulse itself, but also its nearby pulses.

To compute the Wasserstein-1 distance between pulses, we define a level set where the lines are parallel to the x-axis, the y-range is set to $[-0.35, 0.4]$, and the step size of each level is 0.05, that gives 150 levels in total. For pulses x_i and x_j, we compute the cumulative distribution functions F_{x_i} and F_{x_j} of their level sets, then the Wasserstein-1 distance

$$d_{w_1}(x_i, x_j) = \sum_{t=1}^{150} \left|F_{x_i}(t) - F_{x_j}(t)\right|. \tag{7}$$

Figure 4(b) depicts the potential advantage of using Wasserstein-1 distance in Algorithm 1. In the left image of Figure 4(b), the red and green lines represent non-align

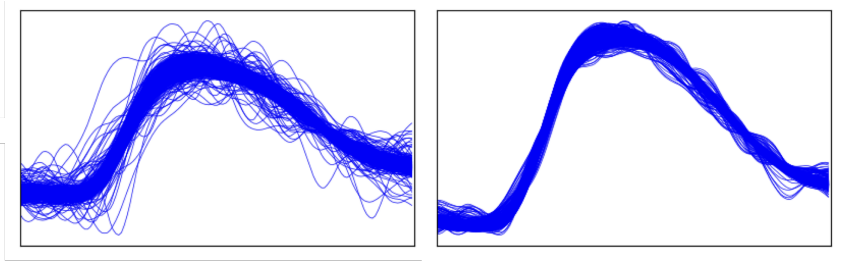

(a) Example of using Hamming window technique. Left: Pulses without windowing. Right: Pulses with Hamming window of $w = 11$.

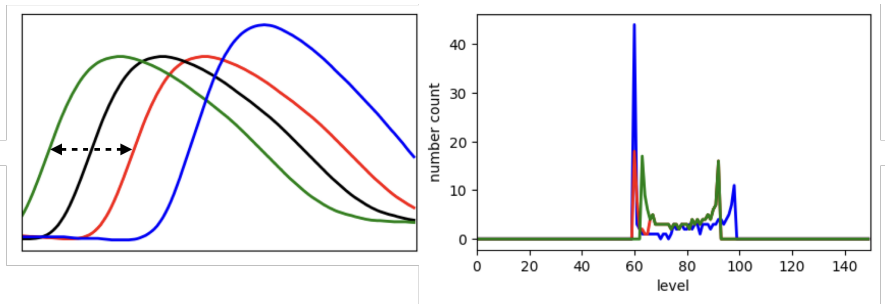

(b) Example of using Wasserstein-1 distance. Left: The red and green lines are non-align pulses, originally located at the black line. The blue line is another pulse. Right: The level sets of the three pulses. Note that the red and green lines coincide after $x = 66$.

Figure 4: Illustration of the two techniques we used to address PPG signal artifacts.

pulses, originally located at the black line, while the blue line represents another pulse. Ideally, the distance between red and green pulses in high-dimensional space should be closer than the distances between both pulses and the blue pulse. This is because the varM of red and green pulses are identical, while the blue pulse is not. When we use Euclidean distance to compute the affinity matrix, the distance between red and blue pulses is 0.68, and the distance between green and blue pulses is 1.32. However, the distance between red and green pulses is 0.86, which is larger than the distance between red and blue pulses. Conversely, when employing Wasserstein-1 distance, the distance between red and blue pulses is 34.50, the distance between green and blue pulses is 52.74, and the distance between red and green pulses is 26.57. Thus, the Wasserstein-1 distances between non-align pulses is smaller than the Wasserstein-1 distances between both non-align pulses and the blue pulse. Notably, the right image of Figure 4(b) displays the level sets of the three pulses, demonstrating that the level sets of the red and green pulses are more similar than the one of the blue pulse, further supporting the aforementioned conclusion.

2.6. Statistical analysis

After obtaining varM of the neohepatic phase of all cases, the Spearman correlation coefficient (CC) is used to measure the linear relationship between varM and the clinical scores. Since the underlying distribution of the indices is unknown, the bias-corrected

and accelerated bootstrap using $100,000$ random samplings with replacement is exploited to establish the 95% confidential interval of each CC. Also, a test of a null hypothesis that the distributions underlying the samples are uncorrelated and normally distributed is performed, and the p-value is reported.

To investigate the effect of the Hamming window technique, we run the procedure on the original dataset, which is obtained directly after the preprocessing, and on another dataset where the Hamming window is applied. We examine the difference between results of Algorithm 1 with affinity matrix using Euclidean distance and Wasserstein-1 distance. Also, we add the results of ABP signal obtained from the previous research to compare the similarity of presentations among ABP and PPG signals. Accordingly, there will be performances of five different models to discuss in this section.

For convenient, we named the five models as follows: model 1 is the case where the original dataset and the Euclidean distance are used; model 2 is the case where the hamming window dataset and the Euclidean distance are used; model 3 is the case where the original dataset and the Wasserstein-1 distance are used; model 4 is the case where the hamming window dataset and the Wasserstein-1 distance are used; and model ABP, which is shown for comparing the results between ABP and PPG signals.

We compare the varM values of five models with the revised Model for End-Stage Liver Disease (MELD_Na) [27, 28] and the early allograft failure (EAF) scores, including L-GrAFT10 [29, 30] and the EASE score [31]. These score systems has been developed by the combination of laboratory examination results to access the liver disease acuity of a patient. The higher the MELD_Na score means higher priority for liver transplant surgery. Similarly, higher L-GrAFT10 and the EASE scores suggest worsen outcome after the transplant surgery. As higher varM is associated with better condition, which means lower clinical scores, the theoretical perfect CC is -1.

2.7. Sensitivity analysis

In the whole procedure, there are two manually chosen parameters: Hamming window size w whenever we uses the Hamming window technique, and trend step size k when calculating trends. Sensitivity analysis is created to exam how variations in the uncertain parameters w and k affect the performances of the procedure, and for testing the robustness of the performance in the presence of uncertainties. Note that when there are two input uncertainties, it involves calculating how much the performance of procedure changes when we make an adjustment to one of its input variables while keeping another as a constant.

3. Result

3.1. Statistical analysis

The results detailed in Section 2.6 are shown in Table 1. The visualization of the CCs and the 95% confidential intervals between varM of five models and clinical scores, including MELD_Na, L-GrAFT10, and EASE score, are presented in Figure 5. Note that the null hypothesis test is consider notable (mark as *) when the p-value is less than 0.01, and is consider significant (mark as **) when the p-value is less than 0.001.

For the four PPG models we performed, using either the technique of Hamming window (model 2) or Wasserstein-1 distance in the DDMap algorithm (model 3) gives

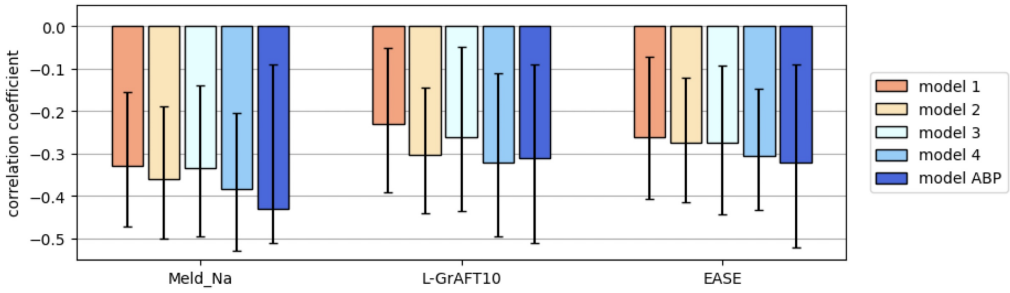

Figure 5: The visualization of the Spearman correlation coefficients and the 95% confidential intervals between varM of five models and three clinical scores.

better results compare to the result of standard procedure (model 1). Most of the time, using only Hamming window is more effective than using only Wasserstein-1 distance. Thus, it is normal to think that using both Hamming window and Wasserstein-1 distance (model 4) gives the best performance, and the results do confirm this conclusion. That is, the performance of model 4 gives best CCs between PPG varM and all three clinical scores. The CCs all exceed -0.3, and the p-values are all notable or significant.

We compare the results of best PPG model (model 4) with the results of model ABP. The CCs between the model 4's varM and the model ABP's varM are all exceptionally similar above our expectation, since their CC differences are only up to a gap of ± 0.05. Note the in the case of L-GrAFT10 score, CC of model 4 even exceed CC of model ABP. Also, the 95% confidential intervals of model 4 are all shorter with respect to model ABP, which indicates a more precise CC of model 4.

Score	Model	Spearman CC	95% Confidential Interval	p-value
Meld_Na	1	-0.329	[-0.47, -0.16]	0.003*
	2	-0.359	[-0.50, -0.19]	0.001*
	3	-0.333	[-0.49, -0.14]	0.002*
	4	-0.384	[-0.53, -0.20]	0.00037**
	ABP	-0.430	[-0.62, -0.21]	0.00005**
L-GrAFT10	1	-0.230	[-0.39, -0.05]	0.038
	2	-0.303	[-0.44, -0.14]	0.006*
	3	-0.261	[-0.44, -0.05]	0.018
	4	-0.321	[-0.49, -0.11]	0.003*
	ABP	-0.310	[-0.51, -0.09]	0.003*
EASE	1	-0.261	[-0.41, -0.07]	0.019
	2	-0.274	[-0.41, -0.12]	0.014
	3	-0.275	[-0.44, -0.09]	0.014
	4	-0.306	[-0.42, -0.15]	0.006*
	ABP	-0.320	[-0.52, -0.09]	0.0033*

Table 1: Detail of the statistical analysis.

3.2. Sensitivity analysis

The sensitivity analysis of these four models is used to test the effect of different trend step size k and Hamming window size w to the four PPG models, and to determine whether the varM are sensitive to the behavior of the chosen parameter. The results of the sensitivity analysis by the CCs between various varM indices of the four models and the Meld_Na score are shown in Figure 6. Note that for model 2 and 4, we first fix $w = 0$ and test the parameter k, which have the same results of testing k for model 1 and 3 respectively. Hence, we skip to show the sensitivity analysis of model 2 and 4 for testing the parameter k. Then, we fix k that provide the best performance and test the parameter w for each two models.

The Spearman correlation between the four models of neohepatic phase and the Meld_Na score are statistical significant among all k from 5 to 129 (Figure 6(c)), expect of model 1 and model 2, which become significant from $k = 9$ (Figure 6(a)). The varM of Model 1 and 3 reaches the best correlation at $k = 25$ and $k = 109$ respectively. As for the Spearman correlation between model 2 and 4 and the Meld_Na score are statistical significant among all w from 5 to 129 (Figure 6(b) and (d)). The varM of Model 2 and 4 reaches the best correlation at $w = 29$ and $w = 21$ respectively.

As for confirming whether the varM show smooth curve for the four models, we use all the differences between adjacent CCs for quantifying the smoothness of the curve. The result of the differences will shown in the form $(a1, [a2, a3], a4)$, where $a1$ is the mean; $[a2, a3]$ is the minimum and maximum; and $a4$ is the IQR. For parameter k of model 1 and 2, the differences between adjacent CCs for the correlations between MELD_Na score and varM are (0.006, [0.0002, 0.018], 0.005); For parameter k of model 3 and 4, the differences are (0.006, [0.0004, 0.054], 0.003); And for parameter w of model 2 and 4, the differences are (0.004, [0.0001, 0.014], 0.004) and (0.006, [0.0004, 0.021], 0.006) respectively. Note that we start from $k = 9$ when calculating differences for parameter k of model 1 and 2, since the CC of $k = 5$ is not statistical significant.

The sensitivity analysis shows that all differences between adjacent CCs are small for the correlations between Meld_Na and the varM of the four models, indicating the varM of all four models achieved consistent correlation and minimal fluctuation from a wide range of parameters k and w. This result concludes that the derivations of the varM of all four models are robust and insensitive to the two input parameters.

4. Discussion

Our results indicate that the variation of the PPG waveform morphology correlates with clinical conditions at a level approaching that of ABP. It suggests that the waveform signal data captured from a noninvasive sensor also possess varM information, which may grant more applications in the future.

4.1. Signal processing perspective

The Hamming window suppresses the fluctuation of the PPG waveform, while the employment of Wasserstein-1 distance alleviate the imperfection of the automatic pulse data isolation. Both provide improved metric for the affinity matrix in DDMap algorithm, which yields the manifold to quantify the variability of morphology.

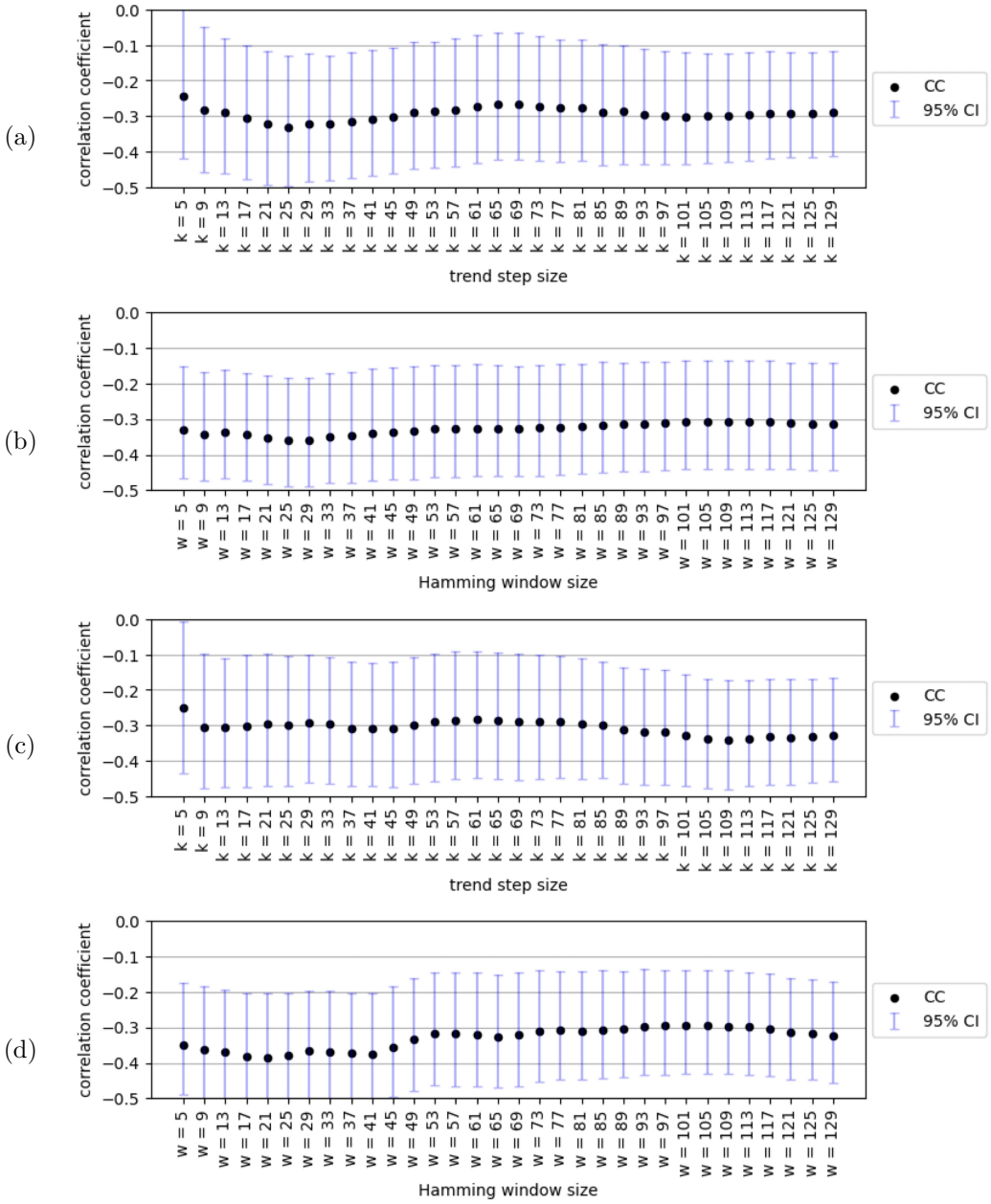

Figure 6: Figure (a) to (d) is the sensitivity analysis of model 1 to 4 respectively, presented by the Spearman correlation coefficients between various varM indices and MELD_Na score.

The DDMap algorithm used to calculate variability of morphology possesses theoretical robustness[3, 12, 11], which has been demonstrated in the sensitivity analysis also[10]. We used DDMap algorithm to extract the variation from the common part of the pulse waveform morphology, the anacrotic phase to the dicrotic phase [6]. Our methodology in this study not only improves performance but also maintains robustness as shown by the sensitivity analysis, which enhances applicability in the future.

It is worth mentioning that our PPG data benefited from several favorable conditions. The consistent anesthetic management throughout the surgery ensured the immobilization, maintained the adequate fluid status of the cardiovascular system, and stabilized the autonomic nerve system, all of which promote a favorable signal acquisition condition. It is important to caution that when employing a PPG sensor for various applications, these factors should be carefully considered. For example, violent physiological responses could be elicited by events such as stressful emotion, hungry or environmental temperature on a healthy human. Under such condition of peripheral vascular constriction, PPG is more susceptible than the direct ABP.

4.2. Biomedical perspective

For clinical perspective, the results of PPG data show that the varM in the neohepatic phase is associated with favorable clinical condition, which is in consistent with the ABP data counterpart in our previous study[10]. As both PPG and ABP signal data are available during the surgery, timely assessment is an advantage over the laboratory examination. The variation in waveform morphology presents both in both ABP waveform and PPG waveform imply other physical modalities of the cardiovascular waveform signal could capture the information, which is intrinsic in physiology. As the pulsatile waveform morphology is the summation of the wave traveling and reflecting throughout the vascular tree, we envision the signal data captured at different sites, whether upper limbs, lower limbs, cervical area, or their combination could provide more versatile application to reveal the human body condition.

The association between varM and clinical condition is reminiscent of heart rate variability (HRV). While similar at first glance, they are different in physiology. The mechanism underlying HRV is mainly the cardiac sympathetic nerve system and the vagal nerve exerting opposite effect on the pacemaker of the heart – the sinoatrial node, while varM could be regulated by the various controlling mechanism of the cardiovascular system, which could include the local blood flow regulation of several visceral organs, and the globalized (and possibly oversimplified) concepts of vascular tone and fluid status. The HRV is the variation of the instantaneous heart rate, an one-dimensional time series, while the successive pulse waveform is multivariate time series, which mandates our methodology[10]. Therefore seeing them as the extensions of the heart rate and blood pressure respectively, we speculate HRV has more direct association to autonomic nerve system while the waveform varM is more related with the cardiovascular system. Despite the differences, there should be intangible physiological interaction between HRV and the varM in cardiovascular waveform. Therefore, we anticipate that the combination of the two may provide a more comprehensive assessment in humans, worthy of future studies.

4.3. Limitation and applicability

Although our PPG results are encouraging, applying varM may encounter practical limitations. The PPG serving as pulse oximeter requires the conditions of adequate

peripheral perfusion and minimal movement during sensor data acquisition. For the best signal quality of PPG waveform, the requirement could be higher. On the other hand, the association between varM and the laboratory examination suggest a possibility assessing the general condition from the signal data. Oftentimes a caregiver would like to judge all available information to assess the latest situation for the best benefit of the patient, while the available information might be limited by the potential harm, the time lag, and the medical resource. It cost minimal based on existential PPG sensor modality while the varM information is imperceptible with naked eye. Our methodology could help provide the caregiver additional piece of information for judgement. We speculate the possibility in sleep medicine or the clinical condition less urgent than the critical care unit. Certainly future studies are required.

5. Conclusion

Via the quantification based on unsupervised manifold learning, beat-to-beat variation of waveform morphology in PPG signal during the liver transplant surgery presents the association with clinical conditions. Signal processing enhancements contribute to the accuracy and robustness of the methodology. Despite practical limitations in PPG signal acquisition, the quantification offers valuable additional information for clinical judgment, potentially supporting patient assessment in various medical contexts. Further research is needed to explore its broader applicability and potential impact on clinical decision-making processes.

6. Acknowledgement

We thank Professor Hau-Tieng Wu (Department of Mathematics, New York University, New York) for the valuable suggetsion on the signal artifact problems that greatly assisted the research. The work is supported by National Science and Technology Council (Taiwan), under research grants 112-2115-M-075-001, and 111-2628-M-A49-008-MY4.

7. Data availability statement

The data that support the findings of this study are available upon request from the authors.

References

[1] Y.-T. Lin, H.-T. Wu, S.-C. Wang, C.-K. Ting, C. Liu, N.-C. Lin, C.-Y. Chen, and C.-C. Loong, "Intraoperative arterial pressure waveforms shows temporal structure complexity correlated with acuity of liver transplant by pulse wave manifold learning analysis," in *Society for Technology in Anesthesia, Virtual Annual Meeting, 2021*, 2021.

[2] S.-C. Wang, H.-T. Wu, P.-H. Huang, C.-H. Chang, C.-K. Ting, and Y.-T. Lin, "Novel imaging revealing inner dynamics for cardiovascular waveform analysis via unsupervised manifold learning," *Anesthesia & Analgesia*, vol. 130, no. 5, pp. 1244–1254, 2020.

[3] C. Shen, Y.-T. Lin, and H.-T. Wu, "Robust and scalable manifold learning via landmark diffusion for long-term medical signal processing," *Journal of Machine Learning Research*, vol. 23, pp. 1–30, 2022.

[4] J.-L. Teboul, B. Saugel, M. Cecconi, D. De Backer, C. K. Hofer, X. Monnet, A. Perel, M. R. Pinsky, D. A. Reuter, A. Rhodes, P. Squara, J.-L. Vincent, and T. W. Scheeren, "Less invasive hemodynamic monitoring in critically ill patients," *Intensive care medicine*, vol. 42, pp. 1350–1359, 2016.

[5] A. P. Avolio, L. M. Van Bortel, P. Boutouyrie, J. R. Cockcroft, C. M. McEniery, A. D. Protogerou, M. J. Roman, M. E. Safar, P. Segers, and H. Smulyan, "Role of pulse pressure amplification in arterial hypertension: experts' opinion and review of the data," *Hypertension*, vol. 54, no. 2, pp. 375–383, 2009.

[6] A. P. Avolio, M. Butlin, and A. Walsh, "Arterial blood pressure measurement and pulse wave analysis—their role in enhancing cardiovascular assessment," *Physiological measurement*, vol. 31, no. 1, p. R1, 2009.

[7] F. Hatib, Z. Jian, S. Buddi, C. Lee, J. Settels, K. Sibert, J. Rinehart, and M. Cannesson, "Machine-learning algorithm to predict hypotension based on high-fidelity arterial pressure waveform analysis," *Anesthesiology*, vol. 129, no. 4, pp. 663–674, 2018.

[8] J. D. Sluyter, A. D. Hughes, C. A. Camargo Jr, S. A. M. Thom, K. H. Parker, B. Hametner, S. Wassertheurer, and R. Scragg, "Identification of distinct arterial waveform clusters and a longitudinal evaluation of their clinical usefulness," *Hypertension*, vol. 74, no. 4, pp. 921–928, 2019.

[9] C. Vlachopoulos, M. O'Rourke, and W. W. Nichols, *McDonald's blood flow in arteries: theoretical, experimental and clinical principles.* CRC press, 2011.

[10] S.-C. Wang, C.-K. Ting, C.-Y. Chen, C. Liu, N.-C. Lin, C.-C. Loong, H.-T. Wu, and Y.-T. Lin, "Arterial blood pressure waveform in liver transplant surgery possesses variability of morphology reflecting recipients' acuity and predicting short term outcomes," *Journal of Clinical Monitoring and Computing*, vol. 37, pp. 1521–1531, 2023.

[11] Y.-T. Lin, J. Malik, and H.-T. Wu, "Wave-shape oscillatory model for nonstationary periodic time series analysis," *Foundations of Data Science*, vol. 3, no. 2, pp. 99–131, 2021.

[12] C. Shen and H.-T. Wu, "Scalability and robustness of spectral embedding: landmark diffusion is all you need," *Information and Inference: A Journal of the IMA*, vol. 11, no. 4, pp. 1527–1595, 2022.

[13] G. Martínez, N. Howard, D. Abbott, K. Lim, R. Ward, and M. Elgendi, "Can photoplethysmography replace arterial blood pressure in the assessment of blood pressure?" *Journal of clinical medicine*, vol. 7, no. 10, p. 316, 2018.

[14] J. Allen, "Photoplethysmography and its application in clinical physiological measurement," *Physiological measurement*, vol. 28, no. 3, p. R1, 2007.

[15] P. A. Kyriacou and J. Allen, *Photoplethysmography: technology, signal analysis and applications.* Academic Press, 2021.

[16] E. Mejia-Mejia, J. Allen, K. Budidha, C. El-Hajj, P. A. Kyriacou, and P. H. Charlton, "Photoplethysmography signal processing and synthesis," in *Photoplethysmography.* Elsevier, 2022, pp. 69–146.

[17] K. Shelley, S. Shelley, and C. Lake, "Pulse oximeter waveform: photoelectric plethysmography," *Clinical monitoring*, vol. 2, 2001.

[18] Y.-T. Lin, Y.-L. Lo, C.-Y. Lin, M. G. Frasch, and H.-T. Wu, "Unexpected sawtooth artifact in beat-to-beat pulse transit time measured from patient monitor data," *PLoS one*, vol. 14, no. 9, p. e0221319, 2019.

[19] M. Elgendi, *PPG signal analysis: An introduction using MATLAB®.* CRC press, 2020.

[20] S. Chatterjee, K. Budidha, and P. A. Kyriacou, "Investigating the origin of photoplethysmography using a multiwavelength monte carlo model," *Physiological measurement*, vol. 41, no. 8, p. 084001, 2020.

[21] M. Elgendi, "On the analysis of fingertip photoplethysmogram signals," *Current cardiology reviews*, vol. 8, no. 1, pp. 14–25, 2012.

[22] P. H. Charlton, P. Celka, B. Farukh, P. Chowienczyk, and J. Alastruey, "Assessing mental stress from the photoplethysmogram: a numerical study," *Physiological measurement*, vol. 39, no. 5, p. 054001, 2018.

[23] M. A. Almarshad, M. S. Islam, S. Al-Ahmadi, and A. S. BaHammam, "Diagnostic features and potential applications of ppg signal in healthcare: A systematic review," in *Healthcare*, vol. 10, no. 3. MDPI, 2022, p. 547.

[24] L. Zelnik-manor and P. Perona, "Self-tuning spectral clustering," in *Advances in Neural Information Processing Systems*, vol. 17, 2004.

[25] L. N. Vaserstein, "Markov processes over denumerable products of spaces, describing large systems of automata," *Problemy Peredachi Informatsii*, vol. 5, no. 3, pp. 64–72, 1969.

[26] J. O. Smith III, *Spectral audio signal processing.* W3K publishing, 2011.

[27] R. S. Brown Jr, K. S. Kumar, M. W. Russo, M. Kinkhabwala, D. L. Rudow, P. Harren, S. Lobritto, and J. C. Emond, "Model for end-stage liver disease and child-turcotte-pugh score as predictors of pretransplantation disease severity, posttransplantation outcome, and resource utilization in united network for organ sharing status 2a patients," *Liver Transplantation*, vol. 8, no. 3, pp. 278–284, 2002.

[28] S. W. Biggins, W. R. Kim, N. A. Terrault, S. Saab, V. Balan, T. Schiano, J. Benson, T. Therneau, W. Kremers, R. Wiesner, P. Kamath, and G. Klintmalm, "Evidence-based incorporation of serum sodium concentration into meld," *Gastroenterology*, vol. 130, no. 6, pp. 1652–1660, 2006.

[29] V. G. Agopian, D. Markovic, G. B. Klintmalm, G. Saracino, W. C. Chapman, N. Vachharajani, S. S. Florman, P. Tabrizian, B. Haydel, D. Nasralla *et al.*, "Multicenter validation of the liver graft assessment following transplantation (l-graft) score for assessment of early allograft dysfunction," *Journal of Hepatology*, vol. 74, no. 4, pp. 881–892, 2021.

[30] V. G. Agopian, M. P. Harlander-Locke, D. Markovic, W. Dumronggittigule, V. Xia, F. M. Kaldas, A. Zarrinpar, H. Yersiz, D. G. Farmer, J. R. Hiatt *et al.*, "Evaluation of early allograft function using the liver graft assessment following transplantation risk score model," *JAMA surgery*, vol. 153, no. 5, pp. 436–444, 2018.

[31] A. W. Avolio, A. Franco, A. Schlegel, Q. Lai, S. Meli, P. Burra, D. Patrono, M. Ravaioli, D. Bassi, F. Ferla *et al.*, "Development and validation of a comprehensive model to estimate early allograft failure among patients requiring early liver retransplant," *JAMA surgery*, vol. 155, no. 12, p. e204095, 2020.